

Spontaneous generation of inertial waves from boundary turbulence in a librating sphere

Alban Sauret¹ †, David Cébron^{1,2} and Michael Le Bars^{1,3}

¹ Institut de Recherche sur les Phénomènes Hors Équilibre, CNRS and Aix-Marseille University, 49 rue F. Joliot-Curie, F-13013 Marseille, France

² ETH Zürich, Institut für Geophysik, Sonneggstrasse 5, CH8092 Zürich, Switzerland

³ Department of Earth and Space Sciences, University of California, Los Angeles, CA 90095-1567, USA

(Received 11 September 2013)

In this work, we report the excitation of inertial waves in a librating sphere even for libration frequencies where these waves are not directly forced. This spontaneous generation comes from the localized turbulence induced by the centrifugal instabilities in the Ekman boundary layer near the equator and does not depend on the libration frequency. We characterize the key features of these inertial waves in analogy with previous studies of the generation of internal waves in stratified flows from localized turbulent patterns. In particular, the temporal spectrum exhibits preferred values of excited frequency. This first-order phenomenon is generic to any rotating flow in the presence of localized turbulence and is fully relevant for planetary applications.

Key words: geophysical and geological flows, rotating flows

1. Introduction

Rotating fluids support so-called inertial waves, which are associated with the Coriolis force (Kelvin 1880). These waves can be directly excited by various harmonic forcings whose frequencies range between plus and minus twice the spin frequency (Greenspan 1968). For instance, Aldridge & Toomre (1969) showed the direct forcing of inertial waves by small periodic oscillations of the spinning rate of a rotating sphere (i.e. "librations") for libration frequencies non-dimensionalized by the mean rotation rate $|\omega_{lib}| \leq 2$ (see also Zhang *et al.* 2013). The nonlinear self-interaction of the excited inertial waves can lead to strong axisymmetric jets, as observed experimentally for tidal forcing (Morize *et al.* 2010). Outside this range of frequencies, inertial waves cannot be excited by direct forcing and were never observed except very recently in an axially librating cylinder in the presence of instabilities near the outer boundary (Lopez & Marques 2011; Sauret *et al.* 2012). The corresponding mechanism is still controversial and is the subject of the present study. We focus here on longitudinal libration in a spherical geometry, which has recently received renewed interest mainly because of planetary applications (e.g. Rambaux *et al.* 2011).

Libration leads to rich dynamics in the contained fluid. At sufficiently large libration amplitudes, centrifugal instabilities are induced near the equator of a sphere where they

† Email address for correspondence: asauret@princeton.edu

generate turbulence (Noir *et al.* 2009; Calkins *et al.* 2010). This instability is generic to any librating container, as for instance in a cylinder (Noir *et al.* 2010; Sauret *et al.* 2012). Libration also induces a mean zonal flow due to nonlinear interactions in the boundary layers even in the absence of inertial waves (Busse 2010; Sauret *et al.* 2010; Noir *et al.* 2012; Sauret & Le Dizès 2013). For libration frequency $|\omega_{lib}| \leq 2$, the dynamic of the fluid becomes more complicated as the contribution of the inertial waves to the mean flow is non negligible. The energy fed to inertial waves is then localized near Ekman-layer eruptions (Calkins *et al.* 2010; Sauret *et al.* 2012; Koch *et al.* 2013). Finally, elliptical instability can also be excited by the libration forcing in ellipsoidal containers (Cébron *et al.* 2012).

In this work, we characterize for the first time the inertial waves excited in a sphere by the boundary flow induced by a longitudinal libration for $\omega_{lib} > 2$. In section 2, we present the governing equations and the numerical methods used to tackle this problem. Then section 3 is devoted to the description of the main numerical results. Taking advantage of the well-known similarities between rotating and stratified flows (e.g. Veronis 1970), those results are finally explained in section 4 in the form of an analytical model extended from closely related studies of internal waves generation from turbulence (Townsend 1966; Dohan & Sutherland 2003, 2005; Taylor & Sarkar 2007).

2. Governing equations and numerical methods

Consider the flow in a sphere of radius R , filled with an incompressible, homogeneous and Newtonian fluid of kinematic viscosity ν and density ρ , rotating about the z -axis at the mean angular velocity Ω_0 . In addition to this mean rotation, the sphere oscillates with an angular frequency ω_{wall} and amplitude $\Delta\Omega$. Using Ω_0^{-1} and R as time and length scales respectively, the instantaneous angular velocity is given by

$$\mathbf{\Omega} = [1 + \epsilon \cos(\omega_{lib} t)] \mathbf{e}_z \quad (2.1)$$

where $\epsilon = \Delta\Omega/\Omega_0$ and $\omega_{lib} = \omega_{wall}/\Omega_0$ are, respectively, the dimensionless libration amplitude and frequency. A schematic of the system is shown in figure 1(a). The dimensionless equations of motion, written in the rotating frame of reference at the mean angular velocity Ω_0 , are

$$\frac{\partial \mathbf{u}}{\partial t} + (\mathbf{u} \cdot \nabla) \mathbf{u} + 2 \mathbf{e}_z \times \mathbf{u} = -\nabla p + E \nabla^2 \mathbf{u}, \quad (2.2)$$

$$\nabla \cdot \mathbf{u} = 0, \quad (2.3)$$

where \mathbf{u} and p are, respectively, the velocity field in the rotating frame of reference and the reduced pressure which takes into account the centrifugal force. There are three governing parameters in our problem: the Ekman number, $E = \nu/(\Omega_0 R^2)$, describing the ratio of the viscous effects and the Coriolis force, ω_{lib} and ϵ . Throughout this study we use the cylindrical polar unit vectors $(\mathbf{e}_r, \mathbf{e}_\phi, \mathbf{e}_z)$. A no-slip boundary condition is used on the outer boundary where $\mathbf{u} = \epsilon \cos(\omega_{lib} t) \mathbf{e}_z \times \mathbf{r}$.

An analogous problem of internal wave generation from turbulence in a stratified flow has shown, by comparison with laboratory experiments, that 2D numerical simulations capture the physical mechanism and key features of internal wave generation (Dohan & Sutherland 2005). Therefore, to be able to reach sufficiently small Ekman numbers, we base our study on axisymmetric simulations. We use a commercial finite element code, Comsol Multiphysics. This numerical model has already been successfully used to study similar problems of libration-driven flows in spherical geometries (Sauret *et al.* 2010; Sauret & Le Dizès 2013) and cylindrical geometries (Sauret *et al.* 2012). For more details

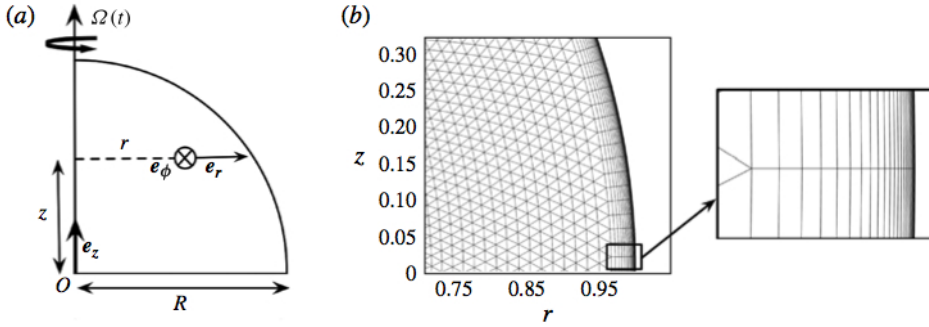


FIGURE 1. (a) Schematic of the upper quarter of the sphere with the cylindrical polar vectors (e_r, e_ϕ, e_z). (b) Mesh grid used in the numerical model showing two zones: a bulk zone with triangular elements and a boundary-layer domain with quadrangular elements. The inset is a zoom of the mesh grid near the outer boundary.

about the numerical procedure and the validation of the numerical code, we refer the reader to Sauret *et al.* (2010). To ensure a high accuracy, all the simulations used in this work are performed with standard Lagrange elements of $P2 - P3$ type (i.e. quadratic for the pressure field and cubic for the velocity field), and the number of degrees of freedom (DoF) used in the simulations is typically of order 350 000. A typical mesh grid is shown in figure 1(b). The mesh grid is composed of 17 794 elements, of which 6 500 are quadrilateral elements devoted to the mesh in the boundary-layer domain and the others are triangular elements for the bulk. More precisely, the boundary-layer domain has a thickness of 0.034 along the outer boundary and is discretized in the direction normal to the boundary into 25 quadrilateral elements with an initial thickness of 5.9×10^{-5} and a stretching factor of 1.2. This ensures that we have a sufficient number of mesh elements in the viscous layer, typically around 13 for the parameters considered in this paper. In addition, the adaptive Backward Differentiation Formula (BDF) order is between 1 and 5 and the time-step leads to more than 500 points per period of libration.

3. Numerical results

3.1. From stable regime to boundary turbulence

In all the following we consider the small Ekman number ($E \ll 1$) and no spin-up regime ($\omega_{lib} \gg \sqrt{E}$), i.e. no spin-up occurs in the bulk at each libration cycle (see e.g. Greenspan 1968; Busse 2010). This situation is satisfied in planetary fluid layers where the Ekman number is typically smaller than 10^{-12} and where the main libration components have frequencies of order 1 (see e.g. Rambaux *et al.* 2011). As shown in figure 2, three flow regimes are observed in the sphere depending on the libration amplitude ϵ (see also Noir *et al.* 2009; Calkins *et al.* 2010). For a libration amplitude ϵ lower than a critical value, called ϵ_{TG} , the flow remains stable and only the viscous layer is visible near the outer boundary; the flow remains laminar everywhere. For $\epsilon > \epsilon_{TG}$ but lower than a critical value, noted ϵ_{turb} , longitudinal rolls, called Taylor-Görtler vortices, develop near the equator along the outer boundary. Then, for an amplitude of libration ϵ larger than the critical amplitude ϵ_{turb} , the longitudinal rolls turn into a turbulent patch localized around the equator. In this last regime, even if the frequency of libration is such that no inertial waves are directly forced (i.e. $\omega_{lib} > 2$), inertial waves are excited in the bulk, emitted from the turbulent patch.

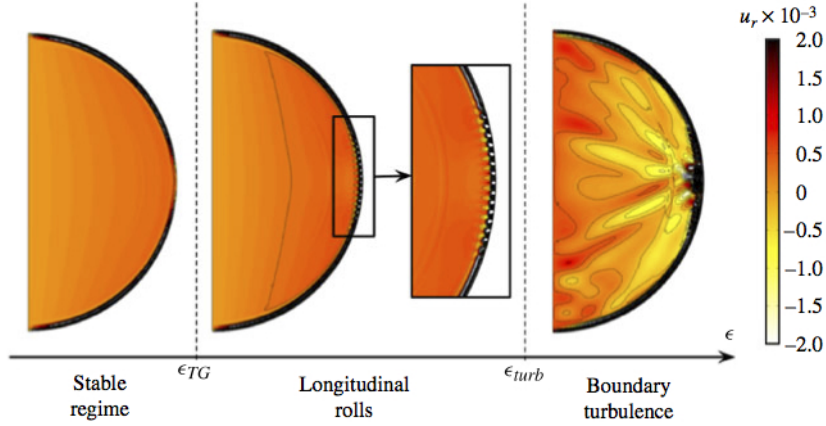


FIGURE 2. Radial velocity u_r in a librating sphere ($\omega_{lib} = 3$, $E = 5 \times 10^{-5}$) for different values of the libration amplitude ϵ (from left to right, $\epsilon = 0.3, 0.55, 0.85$); ϵ_{TG} and ϵ_{turb} are, respectively, the critical value for the appearance of longitude rolls (see the zoom) and boundary turbulence. Spontaneous generation of inertial waves is observed for $\epsilon > \epsilon_{turb}$.

3.2. Characteristics of the generated inertial waves field

To study the generated inertial waves, we performed series of simulations during 30 libration periods (once the permanent regime is reached). An example is shown in figure 3(a) for $\omega_{lib} = 2.1$, $\epsilon = 0.8$ and $E = 4 \times 10^{-5}$, together with the space-time diagram of the radial velocity u_r taken at $r = 0.2$ in figure 3(b). The norm of the two-dimensional Fourier transform of this time series is shown in figure 3(c). It exhibits a patch of large amplitude located at $\omega = 2.1$ and small values of k_z . This patch is directly related to the libration forcing at the frequency $\omega_{lib} = 2.1$. It is due to the velocity variations associated with the Ekman pumping at each libration cycle. In addition to this main frequency, another patch is observed around $\omega \sim 1.6$ and $k_z \sim 2 - 4$, which is the signature of the inertial waves emitted in the bulk. The norm of the Fourier transform averaged over z for $r = 0.2$ is shown in figure 3(d). Again, it clearly exhibits a peak located at the libration frequency $\omega = 2.1$. In addition, it shows a secondary peak around $\omega = 1.4 - 1.6$ as already observed in the cylinder (see Sauret *et al.* 2012).

We have performed the same analysis for other libration frequencies: $\omega_{lib} = 0.1$ (figures 4a,b) and $\omega_{lib} = 3$ (figures 4c,d). In both cases, the norm of the Fourier transform taken at $r = 0.2$ and averaged over z shows a large peak at the libration frequency $\omega = 0.1$ and $\omega = 3$, respectively. For $\omega_{lib} = 3$, the situation is close to the previous case with a peak around $\omega \sim 1.5$. For $\omega_{lib} = 0.1$ a wider range of frequencies is excited in the bulk that may be related to the extended size of the turbulent patch in the Ekman layer. Note also that, in this case, the frequency of libration as well as its higher harmonics $2\omega_{lib}$, $3\omega_{lib}$, ... allow direct forcing of inertial waves. However, the mechanism described above remains fully generic and is superimposed onto these direct forcings, the only difference being that the spectrum is less localized around $\omega \sim 1.4 - 1.6$.

4. Comparison with an idealized analytical model

Following the seminal study of Townsend (1966) and the more recent work of Taylor & Sarkar (2007) for internal waves, the inertial waves propagation in the bulk of the sphere can be understood by a linear model. For the sake of simplicity, we consider here a two-

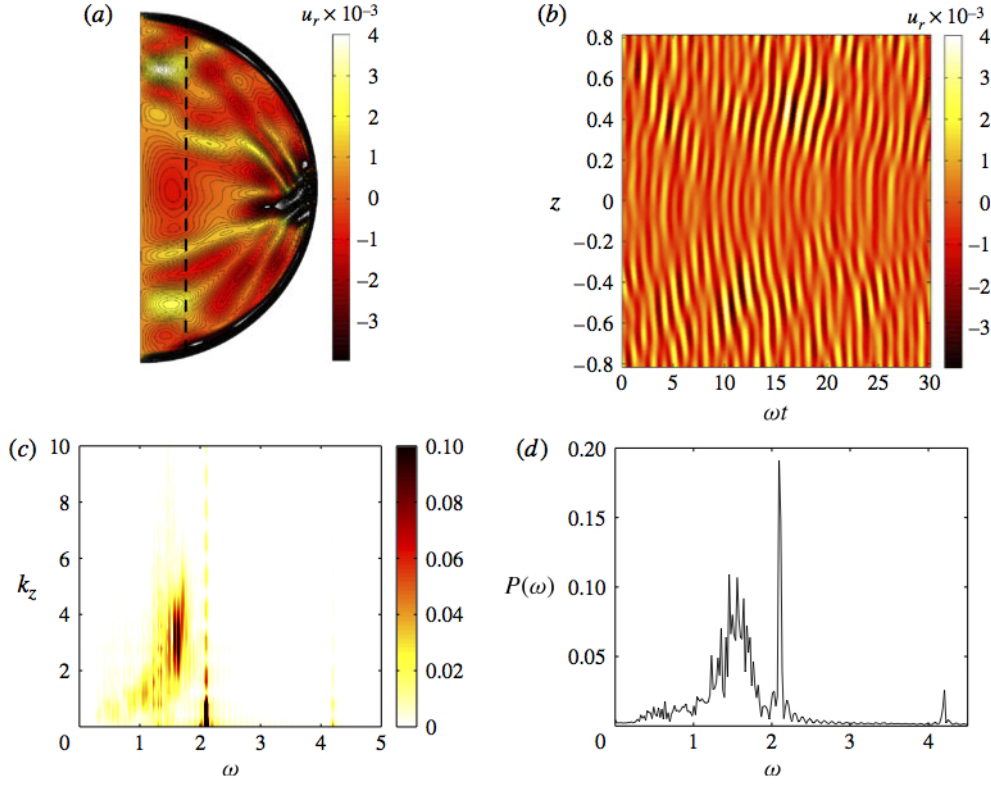


FIGURE 3. Simulations for $\omega_{lib} = 2.1$, $E = 4 \times 10^{-5}$ and $\epsilon = 0.8$. (a) Snapshot of the radial velocity field u_r at $t \equiv 5\pi/(4\omega_{lib})$. (b) Axial time series of u_r as a function of z taken during 30 periods at $r = 0.2$ and corresponding to the simulation shown in figure 3(a) along the dashed line. Apart from the oscillations of the sphere, the propagation of inertial waves is also visible. (c) Corresponding norm of the Fourier transform $P(\omega, k_z)$ showing the axial wavelength and frequency of the generated inertial waves. The colour bar represents $P(\omega, k_z)$. (d) Norm of the Fourier transform of the radial velocity u_r taken at $r = 0.2$ and averaged over z .

dimensional model and neglect the curvature of the boundary of the sphere. In his study of internal waves generated at a horizontal interface, Townsend (1966) considered a gaussian perturbation in both space and time along the horizontal plane $z = 0$ of the vertical displacement, which is directly related to the vertical velocity. Following the analogy between stratified and rotating flows, it is natural to consider here a perturbation of the radial velocity along the plane $r = 1$ and localized around the equator ($r = 1, z = 0$). To perform a tractable analysis, we assume this perturbation to be separable in space and time, i.e.

$$u_r^p(z, t) = f(z) g(t), \quad (4.1)$$

where the spatial function $f(z)$ is maximum at $z = 0$. In the following, owing to the symmetry of the system with respect to the equator of the sphere, we only consider the half-domain $z > 0$. The Fourier transform of the expression (4.1) leads to

$$\hat{u}_r^p(k_z, \omega) = \int \int u_r^p(z, t) \exp[-i k_z z + i \omega t] dt dz = \hat{f}(k_z) \hat{g}(\omega) \quad (4.2)$$

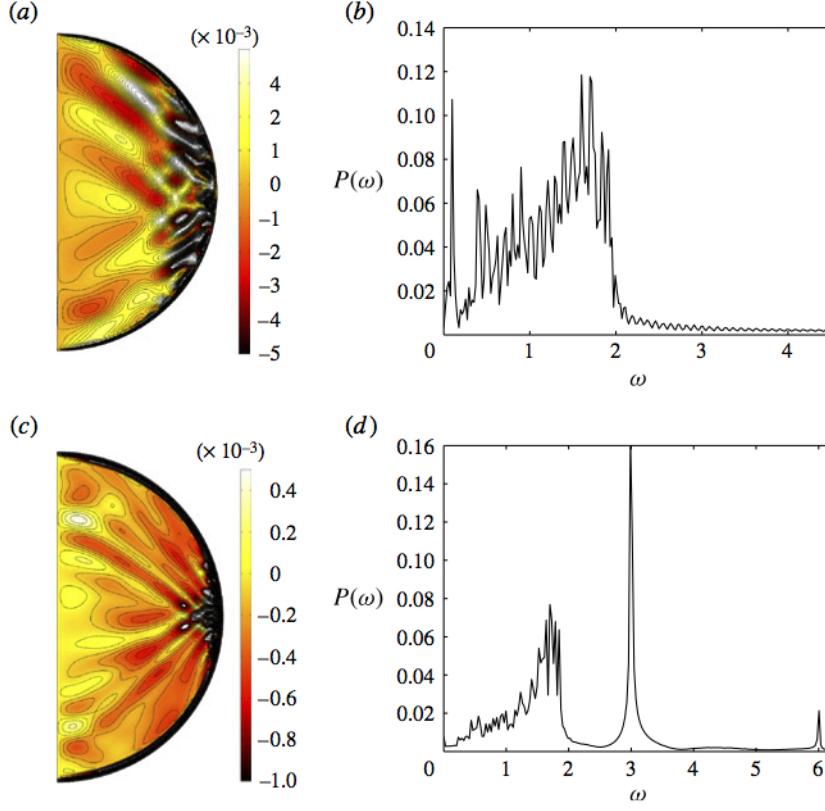


FIGURE 4. Snapshots of the radial velocity field u_r for $E = 4 \times 10^{-5}$, $\epsilon = 0.8$ at (a) $\omega_{lib} = 0.1$ and (c) $\omega_{lib} = 3$. Corresponding norms of the Fourier transform of the radial velocity averaged over z for $r = 0.2$ at (b) $\omega_{lib} = 0.1$ and (d) $\omega_{lib} = 3$.

where $\mathbf{k} = (k_r, k_z)$ is the wavevector and ω is the frequency. The propagation of this perturbation along the r -direction can be written as :

$$u_r(r, z, t) = \frac{1}{4\pi^2} \int \int \hat{f}(k_z) \hat{g}(\omega) \exp[i(k_r(1-r) + k_z z - \omega t)] d\omega dk_z \quad (4.3)$$

The dispersion relation for inertial waves links the axial and radial components of the wavevector:

$$k_r = \pm k_z \sqrt{\frac{4}{\omega^2} - 1} \quad (4.4)$$

The radial velocity field then can be written as

$$u_r(r, z, t) = \frac{1}{4\pi^2} \int_{-2}^2 \hat{g}(\omega) e^{-i\omega t} d\omega \int \hat{f}(k_z) \exp\left[i k_z \left(z \pm (1-r) \sqrt{\frac{4}{\omega^2} - 1}\right)\right] dk_z, \quad (4.5)$$

neglecting the contribution for $|\omega| > 2$, which corresponds to evanescent waves (Greenspan 1968). The relation (4.5) can be rewritten as

$$u_r(r, z, t) = \frac{1}{2\pi} \int_{-2}^2 \hat{g}(\omega) f\left(z \pm (1-r) \sqrt{\frac{4}{\omega^2} - 1}\right) e^{-i\omega t} d\omega \quad (4.6)$$

The temporal Fourier transform of the radial velocity at a position (r, z) is thus

$$\hat{u}_r(r, z, \omega) = \hat{g}(\omega) f\left(z \pm (1-r) \sqrt{\frac{4}{\omega^2} - 1}\right) \quad (4.7)$$

for $|\omega| \leq 2$, with a negligible contribution from $|\omega| > 2$. This expression shows that the signal in the sphere, at first order and neglecting the viscosity, is the product of the temporal signal of the initial excitation $\hat{g}(\omega)$ and the spatial function f . Remembering that this spatial function is localized around 0, the energy in the $z > 0$ space is mainly focused around trajectories

$$z - (1-r) \sqrt{\frac{4}{\omega^2} - 1} = 0, \quad \text{i.e.} \quad \omega = \frac{2(1-r)}{\sqrt{(1-r)^2 + z^2}}. \quad (4.8)$$

This is readily interpreted geometrically. Starting from a point source of fluctuations, waves of all frequencies are emitted with a given amplitude, which depends on the initial excitation in the turbulent patch. Waves with $|\omega| > 2$ are evanescent, while waves with $|\omega| \leq 2$ propagate following the dispersion relation $\omega = 2 \cos \theta$, where θ is the angle of propagation (see e.g. Greenspan 1968). This means that a given point (r, z) can only be reached by a wave having the specific frequency given by (4.8). This geometrical path is plotted in figure 5(a)-(d) for different radial positions and shows good agreement with the numerical results.

To go further, we need the two functions f and g , which can be obtained from simulations. The axial extension of the source, $f(z)$, is well modelled by a gaussian fit, as illustrated in figure 6(a), where we have plotted the maximum amplitude of the fluctuation of the velocity normal to the outer boundary, i.e. the spherical radial velocity. Note that considering the time-averaged velocity normal to the outer boundary leads to a similar lateral extension of the turbulent patch. Taking into account this extension of the source allows one to estimate the extension of the propagating signal around the geometrical path (4.8), taking for instance

$$z - (1-r) \sqrt{\frac{4}{\omega^2} - 1} = \pm \sigma, \quad (4.9)$$

where σ is the standard deviation of the gaussian fit. Results are shown in figure 5(a)-(d) and show good agreement with the numerical results.

A typical temporal Fourier transform of the excitation is shown in figure 6(b). At large frequencies, the turbulent patch is well fitted by a slope ω^{-3} characteristic of a two-dimensional turbulence (see e.g. Smith & Waleffe 1999; Boffetta & Ecke 2012). For $\omega \in [0, 2]$ corresponding to the propagative waves, the norm of the Fourier transform is nearly constant; hence according to (4.7), no frequency is a priori preferred in the bulk. Yet, as seen before, the numerical estimation of the norm of the Fourier transform averaged over z exhibits a maximum, whose location depends on the radial position (see fig. 7). This focalization was also observed in a librating cylinder (Sauret *et al.* 2012) for a turbulent patch localized all along the outer boundary and for the generation of internal waves from a turbulent layer (Dohan & Sutherland 2005; Taylor & Sarkar 2007). In this latter case, the observed frequency selection was attributed to the influence of viscosity. Adapting their study to inertial waves, the viscous attenuation of a given wave with axial wavenumber k_z and frequency ω propagating in the r -direction, is given by

$$\exp \left[-\frac{16 E |k_z|^3}{\omega^4 \sqrt{4 - \omega^2}} (1-r) \right], \quad (4.10)$$

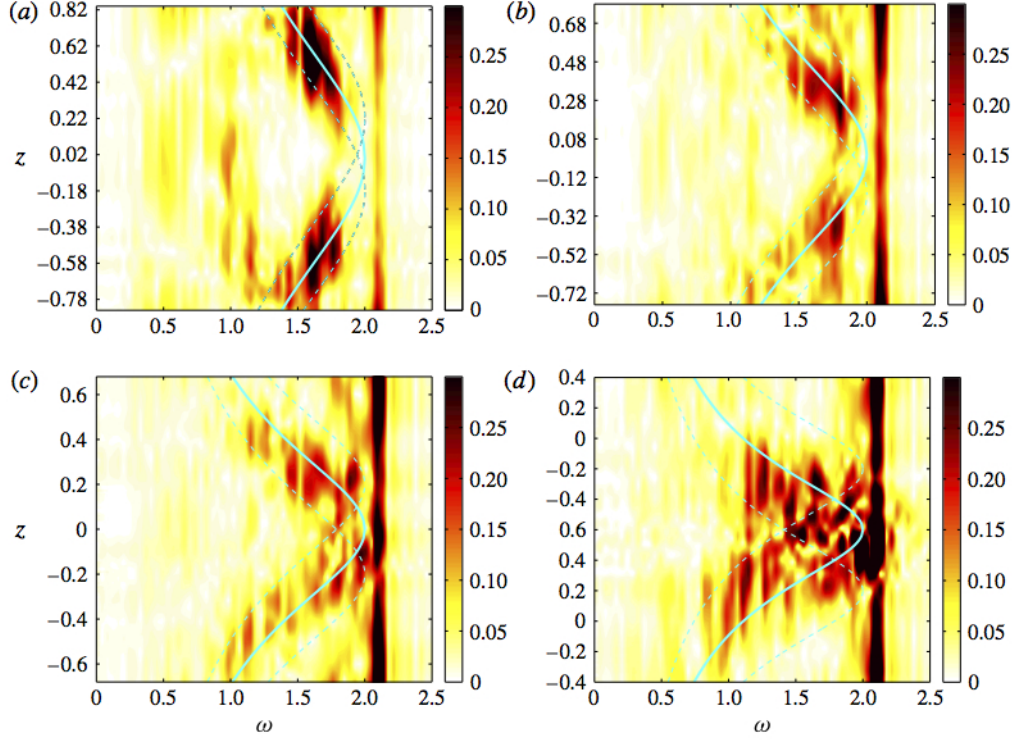


FIGURE 5. Norm of the Fourier transform $P(\omega)$ as a function of z for slices at different radial positions: (a) $r = 0.2$, (b) $r = 0.4$, (c) $r = 0.6$ and (d) $r = 0.8$. The parameters used in the simulations are $\omega_{lib} = 2.1$, $\epsilon = 0.7$ and $E = 4 \times 10^{-5}$. The continuous cyan lines represent the geometrical path given by relation (4.8), and the dashed cyan lines take into account the axial extension of the turbulent patch following (4.9).

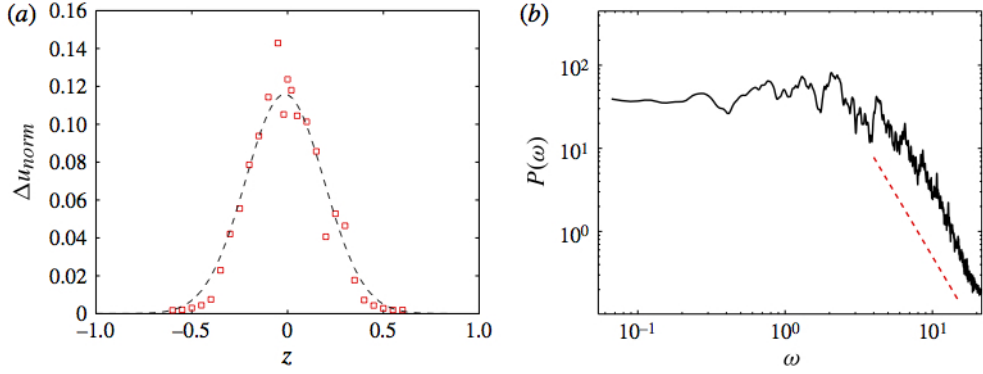


FIGURE 6. (a) Maximum fluctuation of the velocity normal to the outer boundary as a function of z . Parameters are: $\epsilon = 0.8$, $E = 4 \times 10^{-5}$ and $\omega_{lib} = 2.1$. Red squares are the numerical results and the black dashed line is a gaussian fit centered at the equator and of standard deviation $\sigma = 0.2$. (b) Norm of the Fourier transform $P(\omega)$ of the fluctuation of the radial velocity u_r close to the outer boundary ($r = 0.98$, $z = 0$). Parameters are the same as panel (a). The dashed red line shows the slope ω^{-3} .

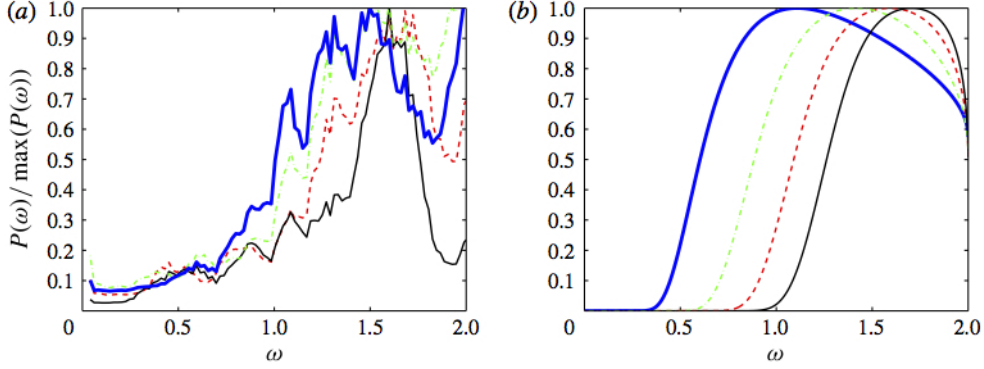


FIGURE 7. Rescaled norm of the Fourier transform $P(\omega)/\max(P(\omega))$ for $\omega \in [0, 2]$ of the fluctuation of u_r at different radial locations averaged over z . (a) Numerical results for $\omega_{lib} = 2.1$ and (b) analytical model plotted with the relation (4.11). We have reported the norm of the Fourier transform at $r = 0.8$ (blue thick line), $r = 0.6$ (green dash-dotted line), $r = 0.4$ (red dashed line) and $r = 0.2$ (black continuous line).

which, according to the typical values considered here (see e.g. figure 3(c)), induces a change in the wave amplitude of less than 0.01%. Viscous attenuation can clearly not account for the frequency selection shown here, and this will be even more true in planetary applications where $E < 10^{-12}$. In the present case, the finite size and the shape of the spherical container are actually responsible for the selection of preferred frequencies. Indeed, using the numerically determined values of the source functions f and g , we can average over z the signal given by the relation (4.7) at a constant r between the boundaries of the sphere $z = \pm\sqrt{1-r^2}$, which gives

$$\langle \hat{u}_r(r, \omega) \rangle_z \propto \left(\operatorname{erf} \left[\frac{(1-r)|k_r/k_z|}{\sigma\sqrt{2}} \right] - \operatorname{erf} \left[\frac{(1-r)|k_r/k_z| - \sqrt{1-r^2}}{\sigma\sqrt{2}} \right] \right) \hat{g}(\omega), \quad (4.11)$$

where erf is the Gauss error function and $|k_r/k_z| = \sqrt{4/\omega^2 - 1}$ (see eq. 4.4). Figure 7 shows the comparison between numerical and analytical results at different radial positions. It exhibits reasonable agreement, taking into account the strong assumptions used in the analytical model. Starting from an excitation localized at the equator and with a flat spectrum between $[0, 2]$, energy is emitted in all directions. But because of geometrical constraints, energy propagation along or close to the direction of the axis of rotation, corresponding to low-frequency waves, is more prevented than propagation along the equator, corresponding to frequencies close to 2. This geometrical frequency selection has a growing importance while going further away from the source, i.e. while r decreases. Hence, while r decreases, selected frequencies are more and more localized close to 2. Note also that the mismatch between the numerical results and the analytical model close to $\omega \sim 2.0$ can be explained by our assumptions. The analytical model is based on a flat excited spectrum in the range $\omega \in [0, 2]$ only. In the numerical simulation, a peak around the frequency $\omega = \omega_{lib} = 2.1$ is also present, associated with the spin-up and spin-down close to the outer boundary at each libration cycle (see also Fig. 3).

5. Conclusion

In conclusion, this work presents the first evidence of spontaneous generation of inertial waves from a localized patch of turbulence in a rotating container and of the related mechanism of frequency selection by geometrical constraints. These processes are illustrated here by a simple two-dimensional analytical model and by simple axisymmetric simulations of a librating sphere. This configuration is especially interesting for planetary applications: celestial bodies such as Io and Europa, are indeed thought to present turbulence around their equator driven by libration (Noir *et al.* 2009). The present mechanism may then participate in the explanation of their preferred eigenmodes of vibration. More generally, we expect the processes presented here to be fully generic to any source of turbulence and to any type of container. A difference must be made between localized and extended patches, as illustrated by the libration of a sphere and of a cylinder for inertial waves. Following the study of Townsend (1966) for internal waves (see also Taylor & Sarkar 2007), the resulting signal for an extended source is equal to the superposition of the effects of random localized sources in space and time. In all cases, a focusing of energy at a given frequency is thus to be expected.

Acknowledgments

D.C. acknowledges support from the ETH Zürich Postdoctoral Fellowship Program and from the Marie Curie Actions for People COFUND Program. M.L.B. acknowledges support from the Marie Curie Actions of the European Commission (FP7-PEOPLE-2011-IOF).

REFERENCES

- ALDRIDGE, K.D. & TOOMRE, A. 1969 Axisymmetric inertial oscillations of a fluid in a rotating spherical container. *J. Fluid Mech.* **37**, 307–323.
- BOFFETTA, G. & ECKE, R. E. 2012 Two-dimensional turbulence. *Ann. Rev. Fluid Mech.* **44**, 427–451.
- BUSSE, F.H. 2010 Mean zonal flows generated by librations of a rotating spherical cavity. *J. Fluid Mech.* **650**, 505–512.
- CALKINS, M.A., NOIR, J., ELDREDGE, J. & AURNOU, J.M. 2010 Axisymmetric simulations of libration-driven fluid dynamics in a spherical shell geometry. *Phys. Fluids* **22**, 086602.
- CEBRON, D., LE BARS, M., NOIR, J. & AURNOU, J.M. 2012 Libration driven elliptical instability. *Phys. Fluids* **24**, 061703.
- DOHAN, K. & SUTHERLAND, B.R. 2003 Internal waves generated from a turbulent mixed region. *Phys. Fluids* **15**, 488–498.
- DOHAN, K. & SUTHERLAND, B.R. 2005 Numerical and laboratory generation of internal waves from turbulence. *Dyn. Atmos. Oceans* **40**, 43–56.
- GREENSPAN, H.P. 1968 *The Theory of rotating fluids*. Cambridge University Press, Cambridge.
- KELVIN, LORD 1880 Vibrations of a columnar vortex. *Phil. Mag.* **10**, 155–168.
- KOCH, S., HARLANDER, U., EGBERS, C. & HOLLERBACH, R. 2013 Inertial waves in a spherical shell induced by librations of the inner sphere: experimental and numerical results. *Fluid Dyn. Res.* **45**, 035504.
- LOPEZ, J.M. & MARQUES, F. 2011 Instabilities and inertial waves generated in a librating cylinder. *J. Fluid Mech.* **687**, 171–193.
- MORIZE, C., LE BARS, M., LE GAL, P., & TILGNER, A. 2010 Experimental determination of zonal winds driven by tides. *Phys. Rev. Lett.* **104**, 214501.
- NOIR, J., CALKINS, M.A., LASBLEIS, M., CANTWELL, J. & AURNOU, J.M. 2010 Experimental study of libration-driven zonal flows in a straight cylinder. *Phys. Earth Planet. Int.* **182**, 98–106.
- NOIR, J., CÉRON, D., LE BARS, M., SAURET, A. & AURNOU, J. M. 2012 Experimental study

- of libration-driven flows in non-axisymmetric containers. *Phys. Earth Planet. Int.* **204–205**, 1–10.
- NOIR, J., HEMMERLIN, F., WICHT, J., BACA, S.M. & AURNOU, J.M. 2009 An experimental and numerical study of librational flow in planetary cores and subsurface oceans. *Phys. Earth Planet. Int.* **173**, 141–152.
- RAMBAUX, N., HOOLST, T. VAN & Ö.KARATEKIN 2011 Librational response of europa, ganymede, and callisto with an ocean for non-keplerian orbit. *A & A* **527**, A118.
- SAURET, A., CÉBRON, D., LE BARS, M. & LE DIZÈS, S. 2012 Fluid flows in a librating cylinder. *Phys. Fluids* **24**, 026603.
- SAURET, A., CÉBRON, D., MORIZE, C. & LE BARS, M. 2010 Experimental and numerical study of mean zonal flows generated by librations of a rotating spherical cavity. *J. Fluid Mech.* **662**, 260–268.
- SAURET, A. & LE DIZÈS, S. 2013 Libration-induced mean flow in a spherical shell. *J. Fluid Mech.* **718**, 181–209.
- SMITH, L. M. & WALEFFE, F. 1999 Transfer of energy to two-dimensional large scales in forced, rotating three-dimensional turbulence. *Phys. Fluids* **11**, 1608.
- TAYLOR, J.R. & SARKAR, S. 2007 Internal gravity waves generated by a turbulent bottom ekman layer. *J. Fluid Mech.* **590**, 331–354.
- TOWNSEND, A.A. 1966 Internal waves produced by a convective layer. *J. Fluid Mech.* **24**, 307–319.
- VERONIS, G. 1970 The analogy between rotating and stratified fluids. *Ann. Rev. Fluid Mech.* **2**, 37–661.
- ZHANG, K., CHAN, K. H., LIAO, X. & AURNOU, J. M. 2013 The non-resonant response of fluid in a rapidly rotating sphere undergoing longitudinal libration. *J. Fluid Mech.* **720**, 212–235.